**EarthArXiv preprint**

# Sparse validation can mask process errors in urban flood modelling:

evidence from large multimodal model-assisted video observations

Shunan Zhou, Heng Lyu, Anette Eltner, Pedro Zamboni,
Nan Wang, Jiaxing Zhao, and Chi Zhang

This manuscript is a preprint submitted to EarthArXiv. It has not been peer reviewed.

Supplementary materials are not included in this preprint version.

Submitting author: Shunan Zhou
ORCID: https://orcid.org/0009-0006-4072-6799

Corresponding author: Heng Lyu
Email: lyuheng@dlut.edu.cn

Preprint version: September 21, 2026

# Sparse validation can mask process errors in urban flood modelling: evidence from large multimodal model-assisted video observations

Shunan Zhou[a,b], Heng Lyu[a,d,*], Anette Eltner[b], Pedro Zamboni[b], Nan Wang[c], Jiaxing Zhao[c], Chi Zhang[a]

[a] *School of Infrastructure Engineering, Dalian University of Technology, Dalian, 116024, China*
[b] *Institute of Photogrammetry and Remote Sensing, Dresden University of Technology, Helmholtzstr. 10, 01069 Dresden, Germany*
[c] *Dalian Municipal Public Security Bureau, Dalian, 116000, China*
[d] *NingBo Institute of Dalian University of Technology, Ningbo, China*

**Abstract**

Urban flood models support drainage-system planning and flood risk management. However, due to the scarcity of monitoring data, model calibration and validation often rely on sparse observations, leaving the process fidelity of models insufficiently assessed. Here, we used large multimodal model-assisted video interpretation to derive minute-level ordinal inundation observations and evaluate the process fidelity of a sparsely calibrated urban flood model. In a case study of Dalian, China, a 1D–2D MIKE FLOOD model was calibrated using five historical peak-depth estimates and validated using three, then evaluated using 20,825 paired simulated and video-derived inundation levels. Direct comparison quantified errors in inundation occurrence, timing, severity, and duration, and two Bayesian cumulative link mixed models characterised their variation across flood phases and rainfall–site conditions. Results showed that although the model achieved low calibration and validation RMSEs of 0.107 and 0.084 m against peak-depth references, video observations revealed its insufficient process fidelity. Simulated onset was delayed by a median of 28.5 min where visible flooding was reproduced, and visible-inundation duration was a median of 29.5 min shorter than observed across all segments. The phase model estimated the highest underestimation probability of 73.6 % during the observation-defined peak phase. Underestimation was also more likely with greater rainfall accumulation over the preceding 30 min, which had the strongest association among the rainfall and site covariates (conditional odds ratio = 6.48). These findings show that sparse peak-depth validation can leave errors in street-scale inundation processes undetected. Future studies should delineate the reliability boundaries of urban flood models using process-informed observations.

*Keywords:* Urban flooding, Inundation dynamics, Large Multimodal models, Surveillance video, Ordinal regression

*Corresponding author.
*Email address:* lyuheng@dlut.edu.cn (Heng Lyu)

## 1. Introduction

Urban flood models represent rainfall–runoff generation, drainage-network flow, and surface inundation to simulate flood occurrence, timing, and severity (Rosenzweig et al., 2021; Guo et al., 2021). Their outputs support flood-risk assessment, drainage-system design, forecasting, and emergency management (Cardoso et al., 2020; Dong et al., 2022; Pathirana et al., 2011). Physically based simulations also supply calibration or training data for reduced-complexity and data-driven surrogate models used for rapid prediction (Löwe et al., 2021; Zahura et al., 2020; Cao et al., 2025). These applications require evidence that simulated flood dynamics are adequate for the decisions they inform.

Credible urban flood models need to faithfully reproduce the location, timing, and severity of inundation across settings and storms. Spatial heterogeneity requires sufficient resolution to represent local differences in flood occurrence, depth, and extent (Qi et al., 2020; Leandro et al., 2016), while rapid urban runoff requires temporal resolution that captures onset, development, peak, persistence, and recession (Cea et al., 2025; Ochoa-Rodriguez et al., 2015). Street-scale predictions are particularly relevant to exposure assessment, traffic control, and emergency response, although city-scale assessments often under-resolve this detail (Xing et al., 2019; Fappiano et al., 2026). Therefore, simulation performance should match the spatial and temporal requirements of the intended application.

However, the observations available for urban flood model calibration and validation often provide limited coverage across locations, times, and inundation states, constraining parameter identification and independent performance assessment (Pirone et al., 2026). We reviewed 25 representative studies of physically based urban flood modelling and identified four observational-constraint profiles (Table 1). First, hydraulic time-series data resolve drainage-system responses but provide limited information on surface inundation and remain spatially sparse. Second, event-maximum surface-flood evidence, including high-water marks, peak depths, and maximum extents, constrains extreme inundation values but contains little temporal information. Third, opportunistic spatial and impact evidence, such as imagery, social-media posts, incident records, and insurance claims, extends coverage of affected locations, with uncertainty in observation timing, spatial attribution, and hydraulic interpretation. Fourth, expert knowledge, disaster reports, and post-event syntheses provide contextual information whose availability and resolution limit

Table 1: Observational constraint profiles identified from a review of 25 representative studies on the calibration and validation of physically based urban flood models. The detailed study-level screening table is provided as Table S1 in the Supplement.

| Observational constraint profile | $n$ | Typical evidence base | Main constraint for validating urban surface-flood dynamics |
|---|---|---|---|
| Hydraulic time-series constraints | 4 | Outlet hydrographs, sewer or manhole water-level series, and surcharge or overflow signatures | Strong temporal constraint on drainage response, rise, recession, and duration, but often indirect for street-scale surface inundation |
| Event-maximum surface-flood constraints | 6 | High-water marks, reported peak depths, mapped maximum extents, flood traces, and peak impact classes | Direct constraint on peak severity and broad wet–dry pattern, with limited leverage on onset, peak timing, and persistence |
| Opportunistic spatial and impact evidence | 12 | Photographs, videos, social-media posts, community reports, incident records, and insurance claims | Broader spatial coverage and hotspot information, but timing, spatial attribution, and hydraulic interpretation are often limited |
| Expert-, report-, or synthesis-based constraints | 3 | Expert and local knowledge, disaster summary reports, historical documents, and post-event syntheses | Provides contextual constraints where instrumental records are scarce, but availability, resolution, and hydraulic specificity are limited |

its use for evaluating detailed surface-flood dynamics. Model evaluation therefore requires observations that combine spatial coverage and temporal continuity with interpretable, sufficiently precise information on local inundation.

Meeting these monitoring requirements simultaneously remains difficult. Achieving enough coverage with fixed sensors requires deployment and maintenance across heterogeneous streets, and local disturbances or data loss can interrupt their records (Tao et al., 2024; Mydlarz et al., 2024). Satellite and UAV observations provide broad coverage, although acquisition timing, weather, and revisit intervals constrain event-long monitoring (Notti et al., 2018; Shastry et al., 2023). For opportunistic images and reports, incomplete information on observation time, location, and hydraulic context limits their integration into model evaluation (Wang et al., 2018; Songchon et al., 2021; Helmrich et al., 2021). Advances in artificial intelligence and visual flood interpretation offer a pathway for extracting inundation information from available imagery (Moy de Vitry et al., 2019; Wang et al., 2024). Large multimodal models (LMMs) further support interpretation of heterogeneous images without task-specific retraining (Lyu et al., 2025; Akinboyewa et al., 2024).

Within this emerging data pathway, fixed-view road-surveillance videos provide repeated observations of flood-prone surfaces and preserve the temporal evolution of inundation (Dale et al., 2026; Hao et al., 2022). Using them for model evaluation requires a common representation in different locations, viewpoints, and events (Zamanizadeh et al., 2025; Notarangelo et al., 2025). Ordered inundation levels provide this representation with reduced dependence on the camera calibration and geometric information required for metric water-depth reconstruction (Wan et al., 2024; Jiang et al., 2019). The resulting sequences support consistent observation–simulation comparisons across sites, storms, and flood phases.

These observations can support a more comprehensive assessment of model fidelity by capturing the evolution of street flooding. Yet, such data have rarely been applied to systematically evaluate urban flood models calibrated under sparse evidence.

This study examines whether sparse validation can mask process errors in urban flood modelling. We aim to address two questions: (1) How faithfully does a peak-depth-calibrated 1D–2D model reproduce the timing, severity, and persistence of street inundation in verified video observations? (2) How do model errors vary across flood phases, rainfall conditions, and urban settings? To this end, we first used GPT-5-assisted interpretation and expert verification to convert 222 site-event videos from 124 sites across five storms in Dalian, China, into 36 490 minute-level ordinal observations. Second, we calibrated and validated a coupled 1D–2D MIKE FLOOD model using historical peak-depth evidence, converted its output to the observational ordinal scale, and paired it with 20 825 observations from 60 sites in the modelled districts. Third, we combined minute-level agreement metrics with segment-scale measures of flood omission, timing, maximum level, and duration to directly quantify discrepancies between simulated and observed inundation. Fourth, we fitted two Bayesian cumulative link mixed models (CLMMs) to diagnose variation in discrepancies across flood phases and their associations with rainfall and site conditions. Together, this design extends evaluation from sparse historical peak depths to observed street-scale inundation sequences.

## 2. Data and Methods

### *2.1. Study area*

The study area is located in Dalian, Liaoning Province, China, a coastal city that has experienced recurrent and damaging summer rainstorms over the past decade, frequently triggering severe pluvial flooding at road intersections, underpasses, and other local depressions. The study area covers approximately 600 $km^2$ and includes steep topographic gradients, dense road networks, commercial buildings, and interspersed green spaces. Drainage is predominantly provided by combined concrete sewers and square conduits, with spatially variable conveyance capacity. Figure 1 shows the full monitoring area, rain gauges, and the two drainage districts represented by the hydrodynamic model.

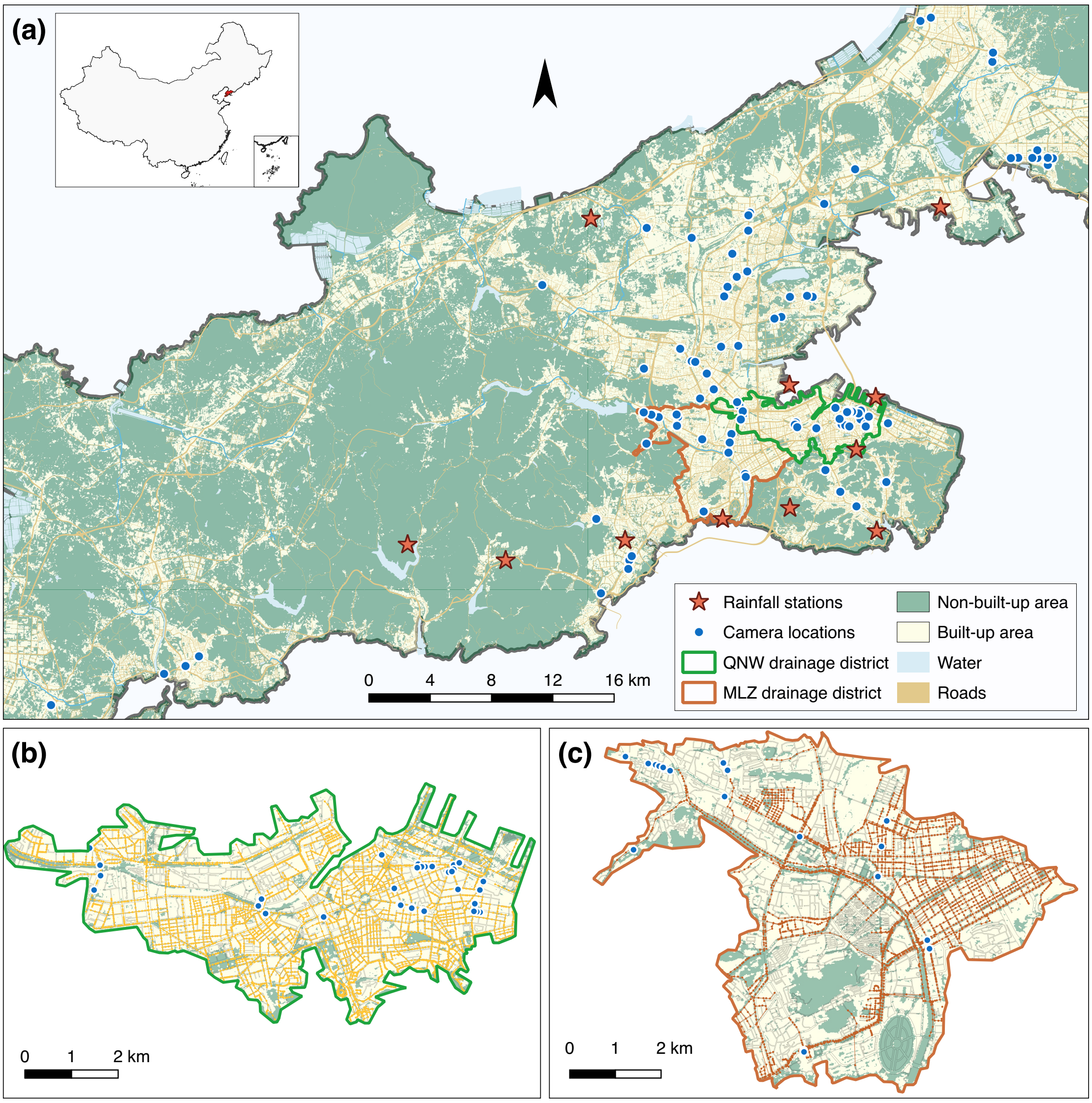


Map data © OpenStreetMap contributors, ODbL (`https://www.openstreetmap.org/copyright`); built-up surface: EMC-BUILT R2025A © European Union, 2025; China boundary data: National Geomatics Center of China.

Figure 1: Study area and monitoring context. Panel (a) shows the location of the study area in Dalian together with the rainfall stations, camera locations, and two modelled drainage districts; panels (b) and (c) show enlarged views of the QNW and MLZ drainage districts, respectively. The modelled districts denote areas where the available stormwater drainage network was included in the coupled model. Roads, waterways, and building footprints were obtained from OpenStreetMap data accessed on 24 May 2025. The built-up background was derived from the 10 m EMC-BUILT R2025A built-up-surface grid for the reference year 2022 (Riffler et al., 2025).

## *2.2. Data*

### *2.2.1. Rainfall events and surveillance records*

Five rainfall events from 2023–2025 were selected to span rainfall amounts, intensities, durations, and spatial patterns, with adequate video coverage at flood-prone locations.

Table 2: Summary of the five rainfall events analysed in this study and the number of event-specific surveillance videos retained for each event. Total rainfall denotes the mean event accumulation across the 11 rain gauges.

| Event date | Total rainfall (mm) | Maximum station-level 1 min intensity ($\mathrm{mm\,min^{-1}}$) | Duration (min) | Videos ($N$) |
|---|---|---|---|---|
| 2023-08-12 | 63.6 | 1.7 | 511 | 54 |
| 2024-07-20 | 17.8 | 1.1 | 271 | 40 |
| 2024-07-26 | 17.6 | 2.1 | 241 | 27 |
| 2024-08-19 | 21.3 | 1.9 | 1 051 | 39 |
| 2025-07-01 | 46.0 | 1.6 | 541 | 62 |

Rainfall observations were obtained from 11 tipping-bucket gauges operated by the Dalian Meteorological Bureau, with all gauges recording at 1 min resolution. Table 2 summarises the event characteristics and surveillance videos.

Municipal departments provided surveillance videos from known hotspots with recurrent urban flooding. Videos were selected based on image quality, visibility, and temporal coverage sufficient to resolve inundation evolution, resulting in an archive of 222 event-specific videos from 124 sites, with site coverage and recording durations varying among events. Subsampling these videos at 1-min intervals yielded 36 490 frames, providing repeated, site-specific observations across events.

### *2.2.2. Covariates for discrepancy analysis*

The discrepancy analysis used two time-varying rainfall descriptors and seven static site attributes. For each monitored site, the nearest rain gauge supplied the 1 min series used to calculate rainfall intensity (I) and accumulation over the preceding 30 min (AR30).

Static site characteristics described local topography, land cover, and drainage or street-network context within the modelled domain. Elevation (ELV), local slope (SLP), and topographic position index (TPI) were derived from the municipal 15 m elevation data. TPI was calculated as the elevation of the central cell minus the mean elevation within a 200 m radius. Imperviousness (IMP) and road density (RD) were derived from OpenStreetMap data accessed on 24 May 2025. RD was calculated as road length in kilometres within a 200 m-radius circle centred on each monitored site, divided by the circle's area in square kilometres. Drainage-network data were derived from the responsible municipal departments, including drainage pipes, outlets, open channels, manholes, and

Table 3: Summary of the rainfall descriptors and site characteristics used in the discrepancy analysis.

| Category | Variable | Description | Unit | Range |
|---|---|---|---|---|
| Rainfall descriptors | I | Instantaneous rainfall intensity | $\mathrm{mm\,min^{-1}}$ | 0–2.1 |
| | AR30 | Antecedent 30 min rainfall accumulation | mm | 0–35.1 |
| Site characteristics | ELV | Elevation | m | 0.58–97.53 |
| | SLP | Slope | % | 0.12–21.22 |
| | TPI | Topographic position index | m | -5.39–8.76 |
| | IMP | Proportion of impervious surface | % | 38.60–99.95 |
| | DMH | Distance to the nearest manhole | m | 3.75–120 |
| | RD | Road length per unit area within a 200 m buffer | $\mathrm{km\,km^{-2}}$ | 0.59–11.32 |
| | DIA | Diameter of the nearest drainage pipe | m | 0.30–2.37 |

their topological connections. Based on these data, the distance to the nearest manhole (DMH) was computed as that from each monitored site to the nearest mapped manhole, and the nearest pipe diameter (DIA) was assigned from the closest mapped drainage pipe. All nine covariates were centred and scaled using their means and sample standard deviations across the paired records. Their definitions, units, and ranges are summarised in Table 3.

### *2.3. Video-based ordinal inundation dataset construction*

Figure 2 summarises the workflow used to convert fixed-view surveillance records into the manually verified ordinal inundation dataset.

GPT-5 assigned inundation levels to the surveillance frames using five ordinal classes (Levels 0–4), from no visible flooding to severe, traffic-disruptive ponding. The classes use stable visual references, including vehicles and pedestrians, following the updated scheme adapted from Lyu et al. (2025). Before inference, privacy-sensitive information and geographic identifiers, including road names, timestamps, and location identifiers, were masked to meet data-sharing requirements and prevent reliance on location cues unrelated to visible flooding. The prompt requested the representative inundation level of the visibly flooded roadway, excluding isolated deeper patches unrepresentative of the road segment. The textual prompt and class definitions are provided in Tables S2 and S3, respectively.

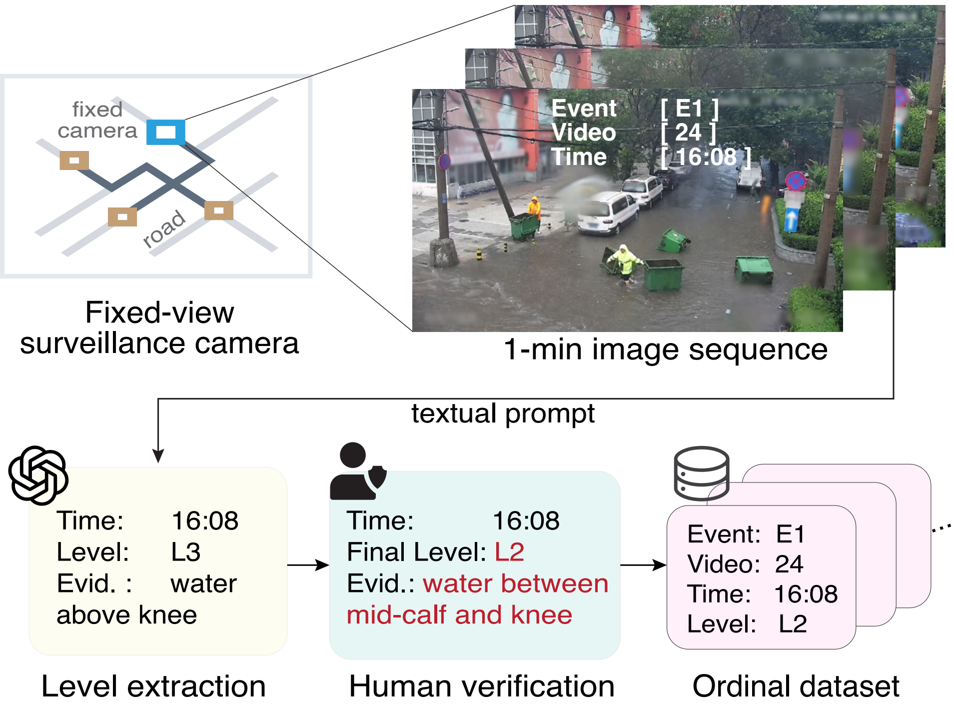


Figure 2: Workflow for constructing the video-derived ordinal inundation dataset. Privacy-masked frames sampled at 1 min intervals were interpreted by GPT-5 using the predefined prompt and ordinal class scheme. Experts reviewed the resulting candidate levels and visual evidence, correcting labels where necessary. The verified levels were then stored with their event, video, and time identifiers. Red text marks the expert correction in the illustrated example.

GPT-5 was accessed through the official OpenAI API, using the snapshot `gpt-5-2025-08-07` (OpenAI, 2025). Batch processing with structured outputs was used to produce a machine-readable response and valid ordinal label for each frame. Each 1 min frame was processed independently, without task-specific fine-tuning or joint multi-frame inference. The temporal consistency and ambiguous cases were assessed during manual verification.

Experts manually verified all 36 490 raw labels before hydrological analysis. For each site-event sequence, they checked labels against the class definitions and visual references, including vehicles, pedestrians, kerbs, and waterlines. Review focused on rain blur, illumination changes, moving vehicles, wakes, and partial occlusion. For ambiguous frames, surrounding minutes were examined to assess consistency with the inundation sequence. Labels were corrected when they contradicted visible evidence or class definitions, or showed abrupt changes unsupported by adjacent frames. The verified labels formed the dataset used for comparison with model outputs.

### *2.4. Coupled 1D–2D urban flood model*

#### *2.4.1. Model configuration*

A coupled 1D–2D model was developed in MIKE FLOOD to simulate rainfall–runoff generation, drainage-network flow, and surface inundation (Patro et al., 2009; Delaney, 2018). The 1D drainage network and 2D surface domain exchanged water bidirectionally through manholes, representing pipe surcharge and surface overflow. Since complete underground drainage data were available only for two districts, the coupled model was restricted to these areas. Consequently, observation–simulation comparisons focused on a subset of 125 event-specific video sequences from 60 sites within the modelled domains. Records with gaps of 2 min or longer were split into distinct continuous segments, yielding 164 segments for subsequent process and phase analyses.

The model was implemented in MIKE FLOOD (version 2014) with a 2D surface grid discretised at a 15 m resolution matching the DEM. Road and green-space cells were lowered by 0.15 and 0.05 m, respectively, and building cells were raised by 10 m to represent urban flow-routing contrasts (Wang et al., 2018; Yang et al., 2023). The outer boundaries of the domain were treated as closed boundaries, and stormwater outfalls discharged freely to receiving waters. Downstream backwater was omitted given the local hilly terrain, frequently dry channels, and upstream reservoir regulation during the simulated storms; such controls are more critical in estuarine or tailwater-controlled drainage settings (Cardoso et al., 2020). Each district received spatially uniform rainfall from its nearest gauge.

#### *2.4.2. Sparse peak-depth calibration and validation*

The model was calibrated against the 2019 flood and validated against the 2020 flood, independently of the video observations used for process evaluation. In the absence of in situ depth monitoring, peak-depth references were interpreted from social-media images (Ming et al., 2025; Smith et al., 2021). Five calibration points and three validation points were available, all in QNW drainage district. The corresponding hyetographs and observed peak depths are provided in Fig. S1 and Table S4. MLZ lacked local rainfall records and depth references for these historical events. To this end, the QNW parameter set was transferred to MLZ based on their proximity and broadly similar topography, land use, and drainage networks. This provided a peak-depth-calibrated baseline under the available observational constraints (Krebs et al., 2016; Singh et al., 2014; Montalvo et al., 2024).

Table 4: Calibration candidates and fixed model settings in the coupled MIKE model.

| Parameter | Meaning | Unit | Value | Calibrated |
|---|---|---|---|---|
| $m_{2d}$ | 2D Manning number assigned to impervious urban-surface cells, controlling effective surface resistance over roads and other impervious areas | $\mathrm{m}^{1/3}\,\mathrm{s}^{-1}$ | 20, 24, 28, 32 | Yes |
| $m_{1d}$ | 1D sewer-pipe Manning number, controlling friction losses in the drainage network | $\mathrm{m}^{1/3}\,\mathrm{s}^{-1}$ | 65, 75, 85 | Yes |
| Inlet area | Effective opening area used in the orifice equation | $\mathrm{m}^2$ | 0.16 | No |
| $C_d$ | Non-dimensional coefficient scaling the 1D–2D orifice exchange discharge | – | 0.65 | No |
| Drying depth | Threshold below which a cell is removed from active flow calculation | m | 0.005 | No |
| Flooding depth | Depth threshold used to reactivate a dry element in the calculation | m | 0.01 | No |
| Wetting depth | Depth threshold above which both mass and momentum fluxes are computed | m | 0.02 | No |
| Eddy viscosity | Sub-grid turbulence or numerical smoothing parameter in 2D flow | $\mathrm{m}^2\,\mathrm{s}^{-1}$ | 1 | No |

Under these constraints, two sensitive roughness parameters–the effective 2D roughness of impervious surface cells and the 1D drainage-pipe roughness–were calibrated using a discrete parameter-grid search. Both parameters used the Strickler coefficient (Manning's $M$, the reciprocal of Manning's $n$), with ranges guided by technical recommendations and previous urban flood applications (Delaney, 2018; Liu et al., 2020; Cardoso et al., 2020). Impervious-surface values of 20, 24, 28, and 32 were combined with pipe values of 65, 75, and 85, yielding 12 combinations evaluated against the peak-depth references. Green-space $M$ remained at the recommended default of 12. Table 4 lists the candidates and fixed settings.

### *2.5. Multi-scale evaluation framework*

Evaluation covered three components: label extraction accuracy against manual verification, model calibration performance against historical peak-depth references, and minute-level and segment-scale discrepancies between observed and simulated inundation processes. Raw GPT-5 labels were compared with verified labels using overall accuracy, class-wise and event-wise recall, and the fraction of errors between adjacent classes. For the historical calibration and validation events, root mean square error (RMSE) and percent bias (PBIAS) quantified peak-depth errors. Formulae for overall accuracy, peak-depth errors, and minute-level agreement are provided in Sect. S3.

For process evaluation, simulated depths were extracted from the nearest 2D grid cell at each monitored site and paired with the verified observations at 1 min timestamps. Camera views covered local road sections, and their locations were checked against the model grid before pairing. Simulated depths were converted to Levels 0–4 using thresholds of 0.01, 0.15, 0.40, and 0.60 m, with values at each threshold assigned to the higher class. These operational thresholds linked continuous simulated depths to the visual classification scheme in Table S3.

Minute-level agreement was assessed using exact accuracy ($\mathrm{Acc_e}$), adjacent accuracy ($\mathrm{Acc_a}$), and quadratic weighted kappa (QWK). Exact accuracy requires identical levels, adjacent accuracy allows a one-class difference, and QWK adjusts for chance agreement while penalising larger ordinal differences more strongly.

Continuous segments were evaluated for onset, peak timing, maximum level, duration, and omitted flooding using Table 5. Visible- and severe-inundation durations counted retained minutes at Levels $\geq 1$ and $\geq 2$, respectively, within the common observation window. Timing errors were calculated for segments in which the simulation reached visible inundation. Omission was summarised by the missed visible-flood rate (MVFR) and missed severe-flood rate (MSFR), each relative to segments with observed flooding at the corresponding threshold. Timing and duration errors were summarised by medians and interquartile ranges (IQRs).

Temporal agreement was also examined in segments with identical simulated and observed maximum ordinal levels. Within this group, onset and duration differences were summarised separately for segments in which both series began and ended at Level 0 and reached Level 1 or above.

Table 5: Process metrics used to compare simulated and observed inundation at the continuous-segment scale. Visible inundation is defined as Level $\geq 1$, and severe inundation as Level $\geq 2$.

| Metric | Definition | Interpretation |
|---|---|---|
| $\Delta T_{\mathrm{onset}}$ | $T_{\mathrm{sim,onset}} - T_{\mathrm{obs,onset}}$; first recorded visible inundation. | $< 0$: earlier simulated onset; $> 0$: delayed simulated onset. |
| $\Delta T_{\mathrm{peak}}$ | $T_{\mathrm{sim,peak}} - T_{\mathrm{obs,peak}}$; first occurrence of the segment maximum. | $< 0$: earlier simulated peak; $> 0$: delayed simulated peak. Computed only when the simulation reached Level $\geq 1$. |
| $\Delta Y_{\mathrm{peak}}$ | $Y_{\mathrm{sim,peak}} - Y_{\mathrm{obs,peak}}$; maximum ordinal level. | $< 0$: peak underestimation; $> 0$: peak overestimation. |
| $\Delta D_{\mathrm{total}}$ | $D_{\mathrm{sim,total}} - D_{\mathrm{obs,total}}$; duration at Level $\geq$ 1. | $< 0$: simulated visible flooding too short; $> 0$: too long. |
| $\Delta D_{\mathrm{severe}}$ | $D_{\mathrm{sim,severe}} - D_{\mathrm{obs,severe}}$; duration at Level $\geq 2$. | $< 0$: simulated severe flooding missed or too short; $> 0$: too long. |
| MVFR | Among segments with observed maximum Level $\geq 1$, the fraction with simulated maximum Level $< 1$. | Complete omission of visible flooding. |
| MSFR | Among segments with observed maximum Level $\geq 2$, the fraction with simulated maximum Level $< 2$. | Complete omission of severe flooding. |

### *2.6. Bayesian cumulative link mixed models for structured discrepancy diagnosis*

Two Bayesian cumulative link mixed models (CLMMs) characterised variation in observation–simulation discrepancies across flood phases and rainfall–site conditions. Their ordinal likelihood preserves category order, while fixed and random effects represent systematic variation and grouped observations (McCullagh, 1980; Hedeker and Gibbons, 1994). Estimated thresholds represent the ordered response categories on the latent scale (Bürkner and Vuorre, 2019; Taylor et al., 2023). Both models used observed inundation level as the response and simulated level as a monotonic predictor. Rainfall-event indicators and model-specific terms represented systematic variation, while site and continuous-segment random intercepts represented persistent local heterogeneity and grouped observations. The flood-phase model characterised variation across observed phases; the rainfall–site model characterised conditional associations with rainfall and site attributes. Both models used the following cumulative-link structure for the observed ordinal response:

$$\Pr\left(Y_{\mathrm{obs},i} \leq m \mid \eta_i\right) = \mathrm{logit}^{-1}(\theta_m - \eta_i)\,, \quad m = 0, \ldots, 3, \tag{1}$$

where $Y_{\mathrm{obs},i} \in \{0, \ldots, 4\}$ denotes the observed inundation level for record $i$, and $m$ indexes the four cumulative cut-points. The ordered thresholds $\theta_m$ separate adjacent response categories, whereas $\eta_i$ is the record-level linear predictor. Under this sign convention, larger values of $\eta_i$ shift probability mass towards higher observed inundation levels.

### *2.6.1. Flood-phase discrepancy diagnosis*

The first CLMM tested whether the observation–simulation discrepancy varied among the rising, peak, and recession phases after accounting for the simulated ordinal baseline and event differences. Flood phase was defined separately within each continuous observation segment from the observed sequence itself. The period before the first occurrence of the segment maximum was labelled *rising*, the period between the first and final occurrence of the maximum observed level was labelled *peak*, and the period after the final maximum was labelled *recession*. For this phase-diagnostic model, the linear predictor was

$$\eta_i^{(\mathrm{phase})} = \mathrm{mo}(Y_{\mathrm{sim},i}) + \beta_{e(i)}^{(\mathrm{Event})} + \beta_{p(i)}^{(\mathrm{Phase})} + b_{\mathrm{site}(i)} + c_{\mathrm{seg}(i)}\,. \tag{2}$$

Here, $\mathrm{mo}(Y_{\mathrm{sim},i})$ denotes the monotonic effect of the simulated inundation level, $e(i)$ and $p(i)$ index the rainfall event and observed flood phase, respectively, and $b_{\mathrm{site}(i)}$ and $c_{\mathrm{seg}(i)}$ are random intercepts for monitoring site and continuous segment. The event of 12 August 2023 served as the reference level for the event fixed effects in both CLMMs. Model performance in each phase was summarised using the posterior probabilities that the simulation underestimated ($Y_{\mathrm{sim}} < Y_{\mathrm{obs}}$), exactly matched ($Y_{\mathrm{sim}} = Y_{\mathrm{obs}}$), or overestimated ($Y_{\mathrm{sim}} > Y_{\mathrm{obs}}$) the observed level, together with the mean ordinal discrepancy $E[\Delta]$, where $\Delta = Y_{\mathrm{obs}} - Y_{\mathrm{sim}}$. Phase-specific predictions were obtained by assigning each phase in turn to all retained records while retaining their simulated levels, event identities, and site and segment effects. Predicted discrepancies were averaged within events and then equally across the five events, and phases were compared using pairwise posterior contrasts. The observation-defined phases served as descriptors of process timing.

### 2.6.2. Rainfall–site discrepancy diagnosis

The second CLMM was designed to diagnose how observation–simulation mismatch varied with rainfall descriptors and local site characteristics after accounting for the simulated ordinal baseline and event-to-event differences. This model excluded the observed phase labels, because they were derived from the response sequence, and instead incorporated the standardised covariates listed in Table 3. Its linear predictor was

$$\eta_i^{(\mathrm{cond})} = \mathrm{mo}(Y_{\mathrm{sim},i}) + \sum_{j=1}^{p} \kappa_j X_{ij} + \beta_{e(i)}^{(\mathrm{Event})} + b_{\mathrm{site}(i)} + c_{\mathrm{seg}(i)}\ , \tag{3}$$

where $X_{ij}$ denotes covariate $j$ for record $i$, and $p = 9$ comprises two rainfall descriptors and seven site characteristics. Conditional on the simulated baseline, event, and random effects, $\kappa_j$ quantifies how a one-standard-deviation increase in covariate $j$ shifts the cumulative log-odds of a higher observed inundation category. The exponentiated coefficients were reported as odds ratios (ORs): values greater than 1 indicate a greater conditional tendency for the simulation to underestimate the observed level, whereas values below 1 indicate the opposite. These ORs describe statistical associations with observation–simulation mismatch, not a causal ranking of physical flood controls. Site-level random intercepts were also expressed as residual ORs to identify localised under- or overestimation remaining after conditioning on the simulated baseline, rainfall–site covariates, and event effects.

### 2.6.3. Model fitting and posterior diagnostics

Both CLMMs were fitted to the same set of 20 825 paired minute-level observation–simulation records. Models were estimated in R using the *brms* package (Bürkner, 2017) with *cmdstanr* as the backend (Gabry et al., 2024). Sampling used the No-U-Turn Sampler with four Markov chains of 3 000 iterations each, including 1 500 warmup iterations. Weakly informative priors were specified as $\mathcal{N}(0, 1)$ for fixed effects, Student-$t(3, 0, 2.5)$ for the ordinal thresholds, and Student-$t(3, 0, 1)$ for the standard deviations of random effects. The maximum tree depth was set to 12 for both models, and the target acceptance probability was set to 0.98 for the flood-phase discrepancy model and 0.97 for the rainfall–site discrepancy model.

Detailed convergence diagnostics, effective sample sizes, divergent-transition checks, posterior category calibration, and in-sample reproduction metrics are reported in Tables S5 and S7. Phase-specific discrepancy probabilities, $E[\Delta]$, and pairwise phase contrasts were summarised by posterior means and 95 % credible intervals (CrIs). Rainfall–site fixed effects, rainfall-event contrasts, and site-level random effects were reported as ORs with 95 % CrIs. OR point estimates were obtained by exponentiating posterior mean coefficients; interval bounds were obtained by exponentiating the corresponding posterior quantiles. Marginal discrepancy curves were generated by varying each selected covariate over its observed range while holding the remaining standardised covariates at zero. These population-level predictions excluded random effects and were averaged over the observed joint distribution of rainfall event and simulated inundation level.

## 3. Results

### *3.1. Video-derived inundation dataset*

#### *3.1.1. Performance of GPT-5 inundation extraction*

Against the expert-verified labels, the GPT-5 extraction achieved an overall accuracy of 0.743 across 36 490 sampled frames. As shown in Fig. 3a, class-wise recalls were 87.3 %, 70.4 %, 70.7 %, 78.7 %, and 88.0 % from Level 0 to Level 4, respectively. Among misclassified frames, 92.5 % differed by one ordinal class. This indicates that the raw GPT-5 outputs generally preserved the correct severity neighbourhood even when the exact label was missed. Ambiguities were concentrated around the Level 0–1 and Level 1–2 boundaries, where illumination, occlusion, vehicle wakes, and shallow water can complicate interpretation. By contrast, severe inundation remained identifiable, with Level 4 recall reaching 88.0 %.

Event-wise class recalls showed similar performance ranges across the five rainfall events (Fig. 3b). Recall ranged from 80.7 % to 92.3 % for Level 0, from 64.0 % to 75.8 % for Level 1, and from 67.0 % to 72.3 % for Level 2. For higher inundation levels, Level 3 recall ranged from 76.2 % to 80.2 % in events where it occurred, while Level 4 recall was 93.5 % on 2024-08-19 and 85.3 % on 2025-07-01. These results indicate that GPT-5 provided an initial classification across events and severity levels for subsequent expert verification.

#### *3.1.2. Coverage of the inundation dataset*

Following expert verification, the dataset covered all five ordinal levels, with most records representing shallow inundation. Level 1 accounted for 22 834 records (62.6 %), followed by Level 0 with 7 592 (20.8 %) and Level 2 with 5 060 (13.9 %). Higher inundation levels occurred less frequently: 628 records were assigned to Level 3 (1.72 %) and 376

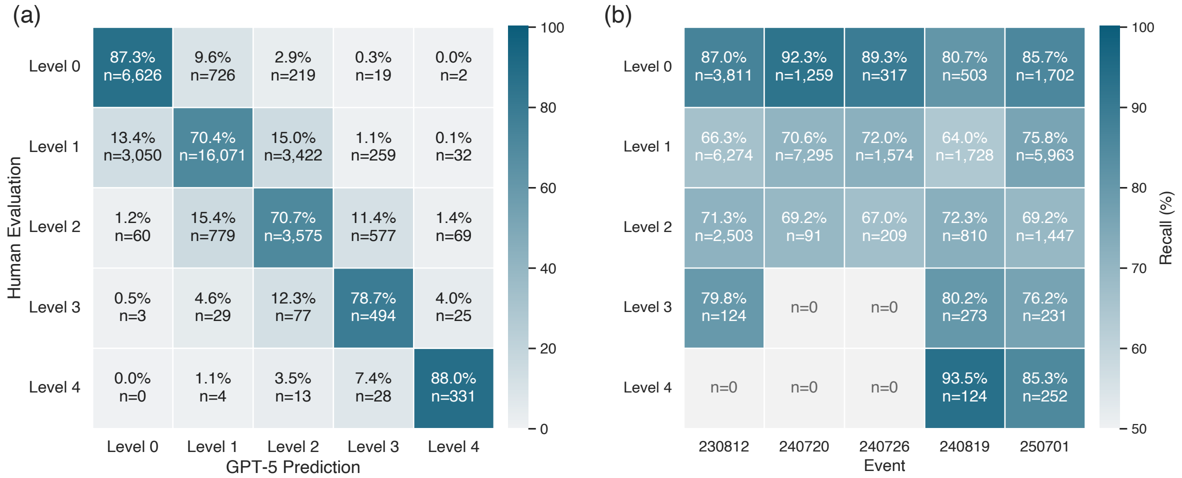


Figure 3: Reliability of the GPT-based inundation extraction before manual verification. Panel (a) shows the confusion matrix of raw GPT-assigned labels against the manually verified labels, and panel (b) shows event-wise class recall, with the number of manually verified frames in each event-class combination reported in each cell.

to Level 4 (1.03 %). The dataset retained information on both common shallow-water conditions and less frequent severe inundation.

The number of records and their severity distribution varied among events. Record totals ranged from 2 100 on 2024-07-26 to 12 712 on 2023-08-12, while the proportion at Level $\geq 2$ ranged from 1.05 % on 2024-07-20 to 35.1 % on 2024-08-19. Level 4 occurred only during the 2024-08-19 and 2025-07-01 events. Usable sequence lengths ranged from 0.4 to 7.9 h, with a median of 2.59 h (Fig. S2). These repeated minute-level records captured variation in inundation severity and persistence across monitored sites and storms.

### *3.2. Model performance under sparse peak-depth and process-based observations*

#### *3.2.1. Model parameter selection*

Figure 4 summarises the calibration performance across the 12 roughness combinations tested in the QNW drainage district and highlights the final parameter selection. The corresponding observed and simulated peak depths at the individual calibration and validation locations are reported in Table S4. The parameter grid revealed a trade-off between reducing RMSE and limiting the magnitude of systematic bias. The 2D impervious-surface roughness controlled most of this trade-off: $m_{2d} = 20$ produced the smallest absolute PBIAS but comparatively high RMSE, increasing $m_{2d}$ to 24 substantially reduced RMSE while retaining moderate bias, and $m_{2d} = 28$ produced a low RMSE but a stronger negative PBIAS. Increasing $m_{2d}$ further to 32 did not improve this compromise.

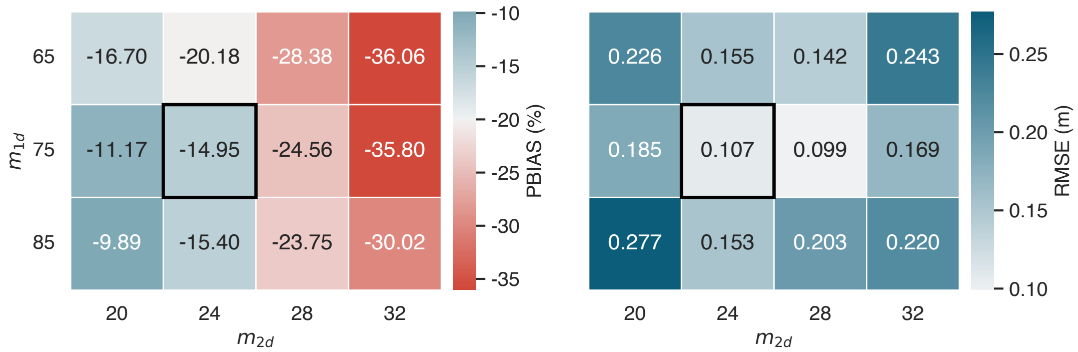


Figure 4: Calibration diagnostics for the 12 tested roughness combinations in the QNW drainage district, based on the five 2019 peak-depth reference points. The left panel shows PBIAS and the right panel shows RMSE. The selected combination ($m_{2d} = 24$, $m_{1d} = 75$) is highlighted.

The influence of the 1D pipe roughness was weaker, although $m_{1d} = 75$ produced the lowest RMSE within the best-performing $m_{2d}$ settings.

The combination $m_{2d} = 24$ and $m_{1d} = 75$ was therefore selected as a compromise between peak-depth error and systematic bias. It yielded a calibration RMSE of 0.107 m and a PBIAS of $-14.95\,\%$ for the 2019 event. Independent validation against the three 2020 peak-depth reference points produced an RMSE of 0.084 m and a PBIAS of $-8.82\,\%$ (Table S4). These aggregate errors established the selected configuration as the conventional peak-depth baseline for the present study. The same parameter set was subsequently transferred to the adjacent MLZ drainage district.

### *3.2.2. Multi-scale discrepancies of the hydrodynamic model*

Evaluation against 20 825 paired minute-level records revealed frequent underestimation of observed inundation despite the small aggregate errors against the peak-depth references. Exact accuracy ($\mathrm{Acc_e}$) was 0.400, adjacent accuracy ($\mathrm{Acc_a}$) was 0.912, and QWK was 0.190. Hence, most records differed by at most one ordinal class, while exact agreement and chance-adjusted ordinal concordance remained limited. Discrepancies were asymmetric: simulated levels were lower than observed in 43.6 % of records and higher in 16.4 %, with one-class underestimation forming the dominant mismatch type (Fig. 5a). The threshold-proximity check further examined how close these one-class underestimates were to the next ordinal boundary in the simulated water-depth series (Fig. S3). Records with simulated Level 0 and observed Level 1 accounted for 85.8 % of one-class underestimates and were all within 1 cm of the next threshold. Median distances were 5.6 cm for simulated Level 1

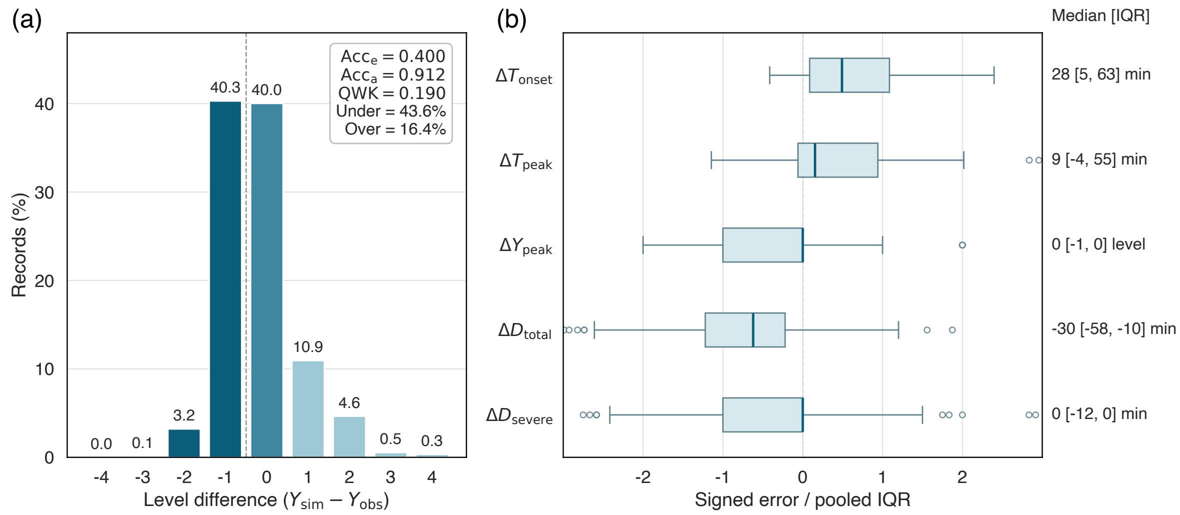


Figure 5: Multiscale diagnostics of the direct comparison between simulated and observed inundation. Panel (a) shows the distribution of minute-level signed discrepancy $Y_{\mathrm{sim}} - Y_{\mathrm{obs}}$, where negative values indicate underestimation by the simulation and positive values indicate overestimation. The pooled $\mathrm{Acc_e}$, $\mathrm{Acc_a}$, and QWK values are also reported. Panel (b) summarises the process-error metrics defined in Sect. 2.5 on an interquartile range (IQR)-standardised axis; for these metrics, negative values indicate earlier, lower, or shorter simulated inundation than observed, whereas positive values indicate later, higher, or longer simulated inundation. Raw medians and IQRs are reported at the right. Time values in the annotations are rounded to whole minutes. Boxes show the IQR with the median as the centre line, and whiskers extend to the most extreme non-outlier values within 1.5 IQR of the quartiles. Severe inundation is defined as Level $\geq 2$. The boxplots use $n = 122$ segments for $\Delta T_{\mathrm{onset}}$ and $\Delta T_{\mathrm{peak}}$, and $n = 164$ segments for $\Delta Y_{\mathrm{peak}}$, $\Delta D_{\mathrm{total}}$, and $\Delta D_{\mathrm{severe}}$. All timing and duration summaries refer to the retained observation windows.

paired with observed Level 2 and 20.2 cm for simulated Level 2 paired with observed Level 3. Thus, the distance to the next threshold varied substantially among mismatch types.

At the segment scale, the discrepancies also involved missed flooding, delayed onset, and shortened inundation duration (Fig. 5b). Visible flooding was missed in 42 of 164 segments (MVFR: 25.6 %), and severe flooding was missed in 45 of 104 segments with observed severe inundation (MSFR: 43.3 %). Among the 122 segments with simulated visible flooding, median onset and peak-timing errors were 28.5 min (IQR: 5–63 min) and 9 min (IQR: −3.5 to 55 min), respectively. Across all 164 segments, the median maximum-level error was 0 classes (IQR: −1 to 0), and median visible-inundation duration error was −29.5 min (IQR: −58 to −10.5 min). Median severe-inundation duration was 8 min in the observations and 0 min in the simulations, consistent with the frequent omission of observed severe flooding.

Table 6: Direct comparison between simulated and observed inundation levels for the five evaluation events. $\mathrm{Acc_e}$, $\mathrm{Acc_a}$, and QWK are computed from all paired minute-level records. The miss rate and process errors are computed at the continuous-segment scale. Median onset and peak-timing errors are summarised only for segments where the simulation reached visible flooding (Level $\geq 1$).

| Event | $\mathrm{Acc_e}$ | $\mathrm{Acc_a}$ | QWK | Missed visible flood (%) | Median $\Delta T_{\mathrm{onset}}$ (min) | Median $\Delta T_{\mathrm{peak}}$ (min) | Median $\Delta Y_{\mathrm{peak}}$ | Median $\Delta D_{\mathrm{total}}$ (min) |
|---|---|---|---|---|---|---|---|---|
| 2023-08-12 | 0.367 | 0.860 | 0.188 | 7.3 | 61.0 | 26.0 | 0 | −17.0 |
| 2024-07-20 | 0.437 | 1.000 | 0.103 | 4.2 | 63.0 | 63.0 | 0 | −116.5 |
| 2024-07-26 | 0.438 | 0.990 | 0.352 | 12.5 | 13.5 | 1.5 | 0 | −35.0 |
| 2024-08-19 | 0.419 | 0.963 | 0.523 | 22.2 | 19.5 | 0.5 | −1 | −19.0 |
| 2025-07-01 | 0.401 | 0.878 | 0.092 | 49.2 | 0.0 | −1.0 | −1 | −23.0 |

These temporal discrepancies persisted in segments with matching simulated and observed maximum ordinal levels. Simulated and observed maximum ordinal levels were identical in 73 of the 164 segments (44.5 %). Within this group, simulated levels were lower than observed in 52.9 % of records during the observation-defined peak phase. In the 20 segments where both series began and ended at Level 0 and reached visible inundation, simulated onset was delayed by a median of 38.5 min and visible-inundation duration was shorter by a median of 62.5 min (Table S6).

Process errors varied among storms (Table 6). The 2024-07-20 event had the largest median visible-duration deficit (−116.5 min) and a median onset delay of 63 min. The 2023-08-12 event had zero median maximum-level error alongside median onset and peak delays of 61 and 26 min. On 2025-07-01, simulations missed visible inundation in 49.2 % of segments. Both 2024-08-19 and 2025-07-01 had a median maximum-level error of −1 class. These results show that timing, duration, and omission errors recurred across storms, with their relative prominence varying by event.

### *3.3. CLMM-based structured discrepancy diagnosis*

Both Bayesian CLMMs showed acceptable overall sampler behaviour and adequate in-sample ordinal reproduction for the diagnostic summaries reported below. Full convergence diagnostics, effective sample sizes, posterior category calibration, and in-sample reproduction metrics are reported in Tables S5 and S7.

#### *3.3.1. Flood-phase concentration of discrepancy*

Within the inundation sequences, the flood-phase CLMM estimated the largest discrepancy for the observation-defined peak phase under the standardised comparison (Sect. 2.6.1;

Fig. 6a,b). For the rising phase, the posterior mean probabilities of simulation underestimation, exact match, and overestimation were 0.243, 0.500, and 0.257, respectively. The mean ordinal discrepancy was −0.05 classes (95 % CrI: −0.05 to −0.03), with underestimation and overestimation probabilities nearly balanced. For the peak phase, the underestimation probability increased to 0.736, the exact-match probability decreased to 0.225, and the mean discrepancy reached 0.97 classes (95 % CrI: 0.96–0.98). This model-adjusted peak-phase estimate corresponds to observed inundation approximately one class higher than simulated under the standardised comparison. Recession had a small negative mean discrepancy of −0.10 classes (95 % CrI: −0.11 to −0.09). Pairwise posterior contrasts placed the peak-phase mean just over one ordinal class above both other phases, identifying a pronounced peak-phase deficit in the simulated inundation levels.

This peak-phase pattern was also evident in the raw event summaries, although its magnitude varied across the five storms (Fig. 6c). Peak-phase mean discrepancies were positive in every event and were largest for 2025-07-01 ($\bar{\Delta} = 0.88$), followed by 2024-08-19 ($\bar{\Delta} = 0.79$) and 2024-07-26 ($\bar{\Delta} = 0.75$). Recession behaviour was more heterogeneous: recession discrepancies were negative for 2023-08-12 ($\bar{\Delta} = -0.98$) and 2025-07-01 ($\bar{\Delta} = -0.23$), but positive for the other three events. These results suggest that peak-phase underestimation recurred across all five storms, while recession errors varied in both magnitude and direction.

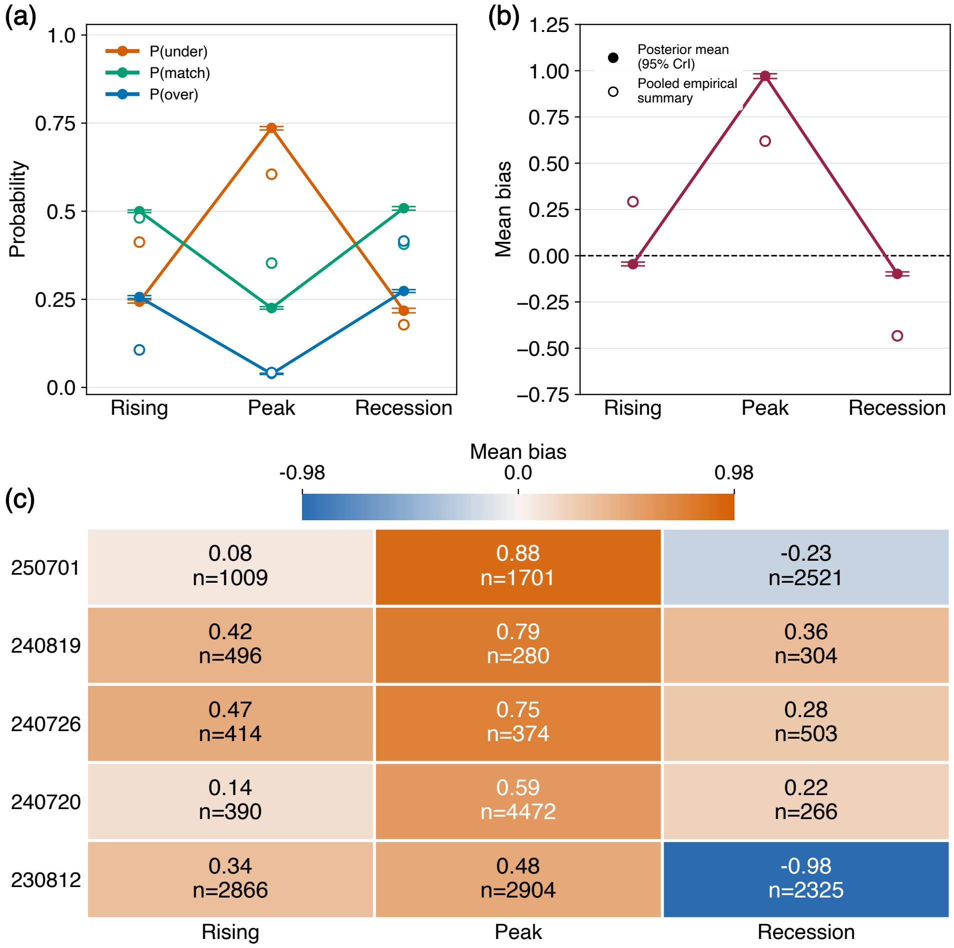


Figure 6: Flood-phase patterns in observation–simulation discrepancy. Panels (a) and (b) show standardised posterior probabilities of simulation underestimation, exact match, and simulation overestimation, and the mean ordinal discrepancy $E[\Delta]$, respectively, from the flood-phase CLMM. Predictions were generated by assigning each phase in turn to all retained records while retaining their simulated levels, event identities, and site and segment effects, then averaged within events and equally across the five events. Filled points and error bars show posterior means and 95 % CrIs; open circles show raw summaries pooled across records within each observed phase. Panel (c) shows the raw mean ordinal discrepancy for each event-phase combination, annotated with the number of paired records. Here, $\Delta = Y_{\text{obs}} - Y_{\text{sim}}$; positive values indicate simulation underestimation and negative values indicate simulation overestimation. Flood phases are defined from the observed sequence.

### *3.3.2. Rainfall–site associations with discrepancy*

The rainfall–site CLMM examined how these discrepancies varied with rainfall and local site conditions after accounting for the simulated inundation level and event differences (Fig. 7). Since all covariates were standardised before fitting, the ORs in Fig. 7a represent the change associated with a one-standard-deviation increase.

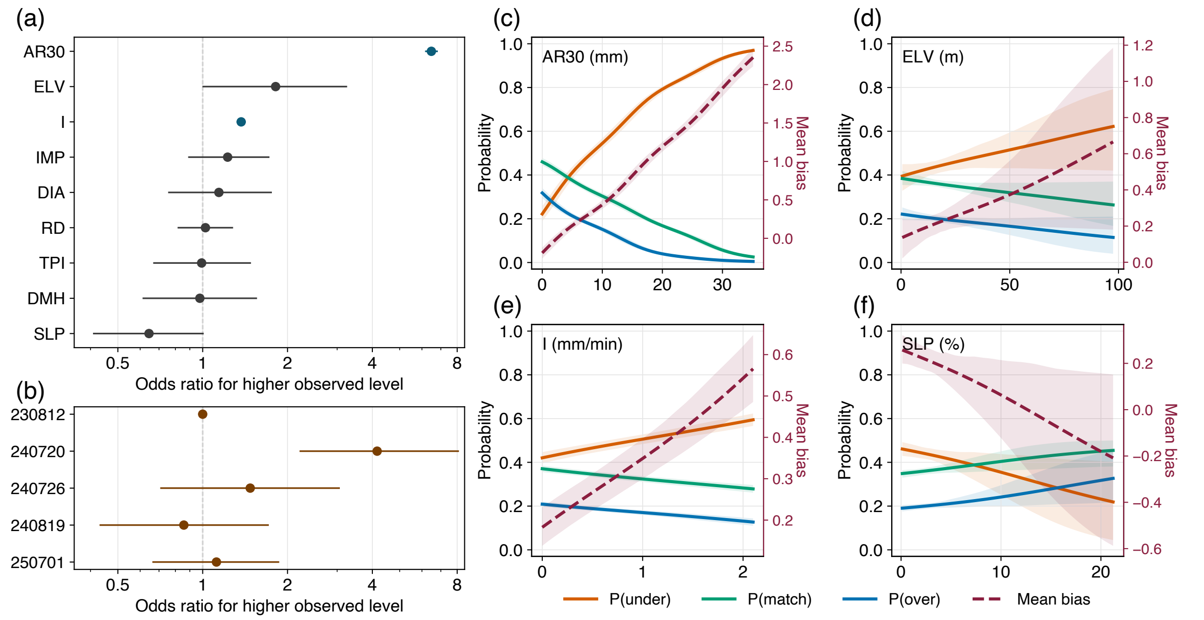


Figure 7: Rainfall–site associations with observation–simulation discrepancy from the rainfall–site CLMM. Panel (a) shows posterior ORs and 95 % CrIs for a one-standard-deviation increase in each continuous covariate. Panel (b) shows rainfall-event fixed-effect ORs relative to the 2023-08-12 reference event. In panels (a) and (b), the vertical dashed line marks an OR of 1. Values greater than 1 indicate higher cumulative odds of a higher observed inundation category, conditional on the simulated level and the remaining model terms, corresponding to a greater tendency for simulation underestimation; values below 1 indicate the opposite. Panels (c)–(f) show marginal discrepancy curves for antecedent 30 min rainfall accumulation (AR30), elevation (ELV), rainfall intensity (I), and slope (SLP). Each focal covariate was varied over its observed range while the remaining standardised covariates were held at zero. Predictions excluded site and segment random effects and were averaged over the observed joint distribution of rainfall event and simulated inundation level. Solid lines show posterior mean probabilities of underestimation ($Y_{\text{obs}} > Y_{\text{sim}}$), exact match ($Y_{\text{obs}} = Y_{\text{sim}}$), and overestimation ($Y_{\text{obs}} < Y_{\text{sim}}$), with shaded bands showing 95 % CrIs. The dashed dark-red line shows the mean ordinal discrepancy, $E[\Delta]$, where $\Delta = Y_{\text{obs}} - Y_{\text{sim}}$. Positive values indicate simulation underestimation and negative values indicate simulation overestimation.

Among the rainfall and site covariates, AR30 had the strongest association with observation-simulation discrepancy. A one-standard-deviation increase in AR30 was associated with 6.48-fold higher conditional odds of simulation underestimation at fixed simulated Levels 0–3 (95 % CrI: 6.15–6.83), holding the other covariates, event, and random effects constant. Across the observed AR30 range, the marginal predictions showed an increase in $P(\text{under})$ from 0.22 to 0.97 and in mean ordinal discrepancy from $-0.19$ to 2.35 classes (Fig. 7c). Rainfall intensity also had a positive association (OR = 1.37, 95 % CrI: 1.32–1.42), with the marginal mean discrepancy increasing from 0.18 to 0.57 classes over its observed range (Fig. 7e). Among the site covariates, elevation had the largest positive point estimate (OR = 1.81, 95 % CrI: 0.999–3.26), with substantially greater uncertainty than the rainfall terms. Slope had a negative point estimate (OR = 0.64, 95 % CrI: 0.41–1.01), with the marginal discrepancy decreasing from positive values at low slopes to negative values at the upper end of the observed range (Fig. 7f). Associations with IMP, DIA, RD, TPI, and DMH were also less clearly resolved, with 95 % CrIs spanning 1.

After accounting for the simulated level and rainfall–site covariates, most differences among rainfall events remained uncertain (Fig. 7b). Relative to 2023-08-12, the 2024-07-20 event had a positive conditional shift (OR = 4.16, 95 % CrI: 2.21–8.12). The CrIs for 2024-07-26, 2024-08-19, and 2025-07-01 overlapped 1.

### *3.3.3. Site-level residual discrepancies*

Site-level random intercepts described the local differences remaining after accounting for the simulated level, rainfall–site covariates, and event effects (Fig. 8a). Across the 60 monitored sites, residual site ORs ranged from 0.29 to 4.75. Most 95 % CrIs crossed 1, none lay entirely below 1, and four lay entirely above 1. These positive residual sites were site 40 (OR = 4.75, 95 % CrI: 1.64–13.46), site 102 (OR = 4.34, 95 % CrI: 1.13–18.43), site 67 (OR = 4.10, 95 % CrI: 1.20–15.15), and site 38 (OR = 2.92, 95 % CrI: 1.005–8.61). All four sites also had positive raw mean observation–simulation discrepancies, with sample support ranging from 183 paired records at site 102 to 780 at site 40.

In the local spatial zooms, sites with elevated residual ORs occurred close to sites with lower estimates, including values below 1 in Fig. 8c. Differences among nearby monitored sites therefore remained after accounting for the simulated level, rainfall–site covariates, and event effects.

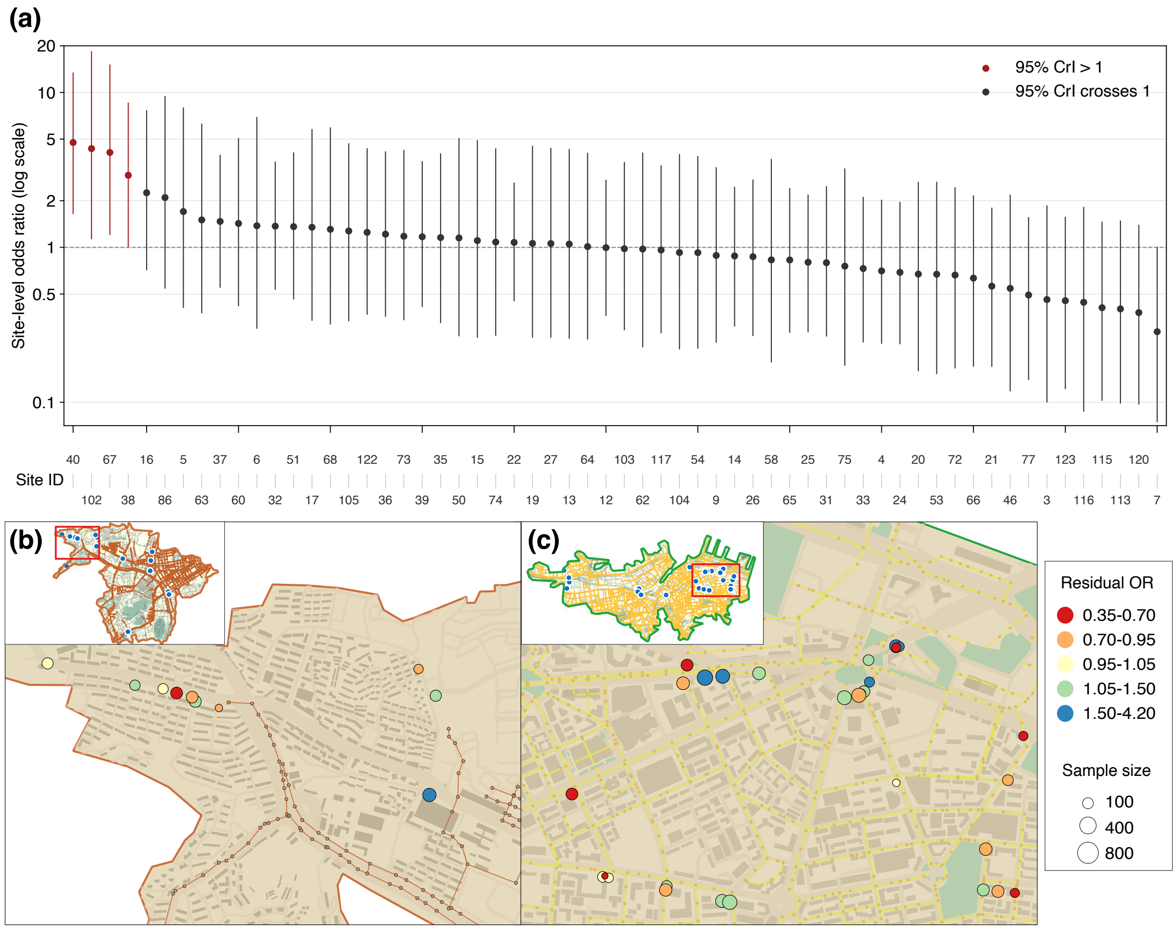




Figure 8: Site-level residual discrepancy after conditioning in the rainfall–site CLMM. Panel (a) shows ranked site-level residual ORs with 95 % CrIs for the 60 monitored sites. The horizontal dashed line marks an OR of 1; values greater than 1 indicate a remaining tendency for the simulation to underestimate the observed level after conditioning on the simulated class, rainfall–site covariates, and rainfall-event fixed effects. Red points denote sites with 95 % CrIs entirely above 1, whereas grey points denote sites whose intervals cross 1. Panels (b) and (c) show two local spatial zooms of the same site-level residual estimates. Each circle represents one monitored site, symbol colour denotes the residual site OR, and symbol size denotes the number of paired minute-level records at that site. Roads and building footprints were obtained from OpenStreetMap data accessed on 24 May 2025.

## 4. Discussion

### *4.1. Process-resolved observations change the interpretation of model credibility*

During urban flood model evaluation, the observational target determines which aspects of model performance are evaluated. The historical references assessed selected peak depths and supplied a conventional calibration and validation baseline (Bennett et al., 2013; Smith et al., 2021). In this study, video sequences revealed additional errors in flood occurrence, onset, and persistence, with underestimation concentrated in the observation-defined peak phase. This phase dependence is consistent with diagnostic approaches that examine model errors during specific periods of the hydrological response (Hsueh et al., 2022).

Segments with matching maximum ordinal levels provided a direct within-window comparison: agreement in maximum severity coexisted with underestimation during the observed peak phase, delayed onset, and shorter inundation duration. These results extend the overall process diagnostics by examining temporal discrepancies within a group whose maximum levels agreed. Timing and persistence influence the effects of street flooding on traffic and access (Yin et al., 2016), giving peak-depth and process-based evaluations complementary roles in model assessment (Pedersen et al., 2022).

### *4.2. Surveillance videos as verified hydrological observations*

Surveillance videos are valuable since they observe the streets and intersections where many pluvial-flood impacts occur. Fixed viewpoints preserve the evolution of local ponding and its surrounding scene at minute-scale resolution (Wang et al., 2019; Costa et al., 2024; Dale et al., 2026). Low-cost ultrasonic networks such as FloodNet demonstrate the value of continuous metric measurements, but they remain sensitive to placement, local obstruction, maintenance, and point-to-area representativeness (Mydlarz et al., 2024). Video records complement these measurements through existing camera coverage and visible scene context.

In this study, GPT-5 made this archive tractable by producing candidate inundation labels for expert verification, yielding 36 490 minute-level observations from 222 site-event videos. Supervised deep-learning models support accurate, rapid interpretation in trained settings, but transfer to new viewpoints, illumination, and flood conditions may require additional task-specific training (Blanch et al., 2026; Wang et al., 2024; Notarangelo et al., 2025; Akinboyewa et al., 2024). Here, GPT-5 supplied initial labels without task-specific training, and expert review established the final observational record. This division of work combined scalable initial interpretation with scene-based checking of ambiguous flood states.

### *4.3. Hydrological meaning of structured model discrepancies*

The phase diagnostics identified the observation-defined peak phase as the period with the greatest underestimation. Model-adjusted rising-phase mean discrepancies were small, and recession behaviour varied among events. This pattern makes the timing and persistence of high inundation levels a priority for model evaluation, alongside the maximum level reached within each observed segment.

The rainfall–site CLMM associated greater antecedent 30 min rainfall with higher conditional odds of simulation underestimation. This association was stronger than that for rainfall intensity, identifying recent rainfall accumulation as a useful condition for examining when the simulated response departs from the observations. Rainfall assignment, drainage conveyance, surface storage, and routing are relevant components to examine under these conditions (Cristiano et al., 2017; Ochoa-Rodriguez et al., 2015; Hossain Anni et al., 2020). Among the site attributes, elevation had the largest positive point estimate for its association with underestimation (OR = 1.81), making terrain representation a useful focus for further diagnosis. The model's 15 m elevation data may not fully resolve kerbs, road crowns, small depressions, and local drainage pathways that influence the routing and storage of surface water. Higher-resolution terrain data and site surveys could improve the representation of these features and underpasses (Techapinyawat et al., 2023). Comparing the resulting inundation sequences would help assess how much the diagnosed discrepancies respond to improved terrain representation and which persist under the existing drainage configuration and parameterisation (Yang et al., 2023; Wang et al., 2018; Fappiano et al., 2026).

Four sites showed positive site-specific shifts after accounting for the simulated level, rainfall–site covariates, and event effects. These locations provide priorities for checking drainage connectivity, road geometry, terrain representation, and observation–simulation alignment (Montalvo et al., 2024). The conditional associations identify times, rainfall conditions, and locations for closer model evaluation. Attribution to forcing, drainage representation, or parameterisation requires further comparisons. In this work, the phase and rainfall–site models provide complementary diagnoses of these patterns through separately fitted predictor sets.

### *4.4. Implications for urban flood calibration and observation design*

The present MIKE FLOOD configuration provides a baseline calibrated against sparse peak depths, yet its parameterisation remains weakly constrained. The peak-depth references supported selection of the two roughness parameters and an independent validation, but did not directly constrain inundation timing and persistence. Roughness choices may interact with structural representations of inlet exchange, local storage, and drainage connectivity, allowing similar peak-depth errors to coexist with different process behaviour. This creates the potential for equifinality: a model may pass a sparse check while retaining parameter or structural deficiencies that emerge only when the full flood sequence is examined (Beven and Freer, 2001; Liu et al., 2020; Huang et al., 2022).

Verified video observations provide a way to move from post-calibration checking to process-informed calibration. Rather than using video only as external diagnostic evidence, process-informed multi-objective calibration methods could incorporate threshold exceedance, onset and peak timing, inundation duration, and peak-stage ordinal severity alongside conventional depth-error metrics (Shahed Behrouz et al., 2020). Such methods would test whether process observations better constrain parameter selection or instead expose input and structural limitations that cannot be resolved through parameter adjustment.

The diagnostics also inform observation design. Additional cameras, field checks, rainfall measurements, drainage surveys, or temporary sensors should be prioritised where the present analysis points to unresolved model behaviour, including periods and locations with strong rainfall-associated discrepancies, peak-phase deficits, and residual site hotspots. The strong AR30 association motivates us to conduct closer examination of the district-wide single-gauge forcing used in the hydrodynamic model. Comparisons with spatially interpolated gauge fields, denser rain-gauge observations, or higher-resolution rainfall products could assess whether spatial rainfall variability contributes to the observed discrepancies. Pairing rainfall-input comparisons with improved terrain and drainage information would help separate forcing uncertainty from limitations in local physical representation (Yu et al., 2025). In this sense, the verified video sequences provide a common record for assessing how these changes affect flood dynamics.

### *4.5. Limitations and future directions*

Three limitations define the scope of the present findings. First, the camera sample was derived from known or historically recognised waterlogging hotspots, so the dataset should be interpreted as a targeted diagnostic sample. Second, the ordinal scale provides a common basis for comparing heterogeneous video-based observation and simulation, but it cannot resolve sub-class water-depth differences. Third, the CLMMs provide diagnostic associations rather than causal decomposition, so the effects of rainfall forcing, terrain inputs, drainage representation, model structure, and parameterisation need to be isolated through further experiments.

Future work should pursue three directions. First, process-informed multi-objective calibration should incorporate the verified inundation sequences into parameter selection and assess the resulting performance across storms and sites. Second, local model checks should combine finer terrain, more complete drainage information, improved rainfall forcing, and targeted surveys at sites with additional positive conditional shifts. Third, metric-depth estimation should combine paired water-level measurements with camera calibration and photogrammetric methods at suitable viewpoints. Reference objects, surveyed control points, road-surface models, and water-edge interpretation could link ordinal classes to metric depths and resolve within-class variation (Dale et al., 2026; Zamanizadeh et al., 2025).

## 5. Conclusions

This study assessed the process fidelity of a sparsely calibrated urban flood model using surveillance-video observations in Dalian, China. GPT-5-assisted interpretation and manual verification produced minute-level ordinal inundation records from five storms. These records were used to evaluate a coupled 1D–2D MIKE FLOOD model calibrated and validated against historical peak-depth references. Multi-scale comparisons and Bayesian CLMMs were applied to 20 825 observation–simulation pairs to assess process fidelity and diagnose systematic discrepancies.

The model achieved low aggregate errors against the historical peak-depth references, yet exact agreement with the paired video observations was only 0.400. Simulations missed visible flooding in 25.6 % of segments with observed visible inundation and severe flooding in 43.3 % of segments with observed severe inundation. Where visible flooding was reproduced, simulated onset was delayed by a median of 28.5 min; across all segments, visible-inundation duration was a median of 29.5 min shorter than observed. Delayed onset and shortened duration also persisted in segments with matching simulated and observed maximum ordinal levels. Thus, agreement in maximum severity provided limited information about whether the model reproduced the timing and persistence of inundation.

The flood-phase CLMM identified the observation-defined peak phase as the period of greatest underestimation, with a standardised underestimation probability of 73.6 % and a mean deficit of 0.97 ordinal classes. The rainfall–site CLMM showed that underestimation was more likely with greater rainfall accumulation over the preceding 30 min, which had the strongest association among the rainfall and site covariates (OR = 6.48 per standard-deviation increase). Among the site attributes, elevation had the largest positive point estimate (OR = 1.81). After accounting for the simulated level, rainfall–site covariates, and event effects, four sites had residual ORs with 95 % CrIs above 1, indicating additional local underestimation.

Process-resolved video observations revealed temporal and conditional errors that were not apparent from sparse peak-depth validation. The combined evaluation may help delineate model credibility across flood phases, rainfall conditions, and locations by identifying departures from observed inundation. Future work should incorporate these sequences into calibration and use them to assess how changes in rainfall forcing, terrain data, and drainage representation affect the simulated inundation process.

## Data and code availability

The code and derived data supporting this study are publicly available from Zenodo (Zhou and Lyu, 2026). The repository contains the code for the CLMM analyses, the expert-verified video-derived ordinal inundation observations, and the panel dataset linking model simulations, matched observations, rainfall and site attributes. A version corresponding to the manuscript will be maintained in the repository. Raw surveillance videos cannot be made publicly available because they originate from third-party monitoring systems.

## CRediT authorship contribution statement

**Shunan Zhou:** Conceptualization, Data curation, Formal analysis, Methodology, Validation, Software, Writing – original draft, Writing – review and editing. **Heng Lyu:** Funding acquisition, Project administration, Supervision, Writing – review and editing. **Anette Eltner:** Methodology, Validation, Supervision, Writing – review and editing. **Pedro Zamboni:** Conceptualization, Methodology, Software, Writing – review and editing. **Nan Wang:** Resources, Writing – review and editing. **Jiaxing Zhao:** Resources, Writing – review and editing. **Chi Zhang:** Supervision, Funding acquisition, Writing – review and editing.

## Declaration of competing interest

The authors declare that they have no competing interests.

## Declaration of generative AI and AI-assisted technologies in the manuscript preparation process

AI tools were used to support the development and debugging of scripts used in the Bayesian CLMM analyses and for generating figure code. These tools were not used to formulate the research questions, define the scientific interpretation, make methodological decisions, or draw the conclusions. All code, analyses, figures, manuscript text, interpretations, and conclusions were reviewed, edited, and verified by the authors, who take full responsibility for the content of this work.

## Funding

This work was supported by the National Key R&D Program of China (grant no. 2024YFC3213000), the National Natural Science Foundation of China (grant no. 52309005), and the China Scholarship Council (CSC; grant no. 202506060152).

## Acknowledgements

We thank the Dalian Municipal Public Security Bureau for supporting access to the surveillance-video records and associated urban flood information used in this study. We also thank the Dalian Meteorological Bureau for providing the rainfall observations.

## References

Akinboyewa, T., Ning, H., Lessani, M.N., Li, Z., 2024. Automated floodwater depth estimation using large multimodal model for rapid flood mapping. Computational Urban Science 4, 12. doi:10.1007/s43762-024-00123-3.

Bennett, N.D., Croke, B.F., Guariso, G., Guillaume, J.H., Hamilton, S.H., Jakeman, A.J., Marsili-Libelli, S., Newham, L.T., Norton, J.P., Perrin, C., Pierce, S.A., Robson, B., Seppelt, R., Voinov, A.A., Fath, B.D., Andreassian, V., 2013. Characterising performance of environmental models. Environmental Modelling & Software 40, 1–20. doi:10.1016/j.envsoft.2012.09.011.

Beven, K., Freer, J., 2001. Equifinality, data assimilation, and uncertainty estimation in mechanistic modelling of complex environmental systems using the glue methodology. Journal of Hydrology 249, 11–29. doi:10.1016/S0022-1694(01)00421-8.

Blanch, X., Grundmann, J., Hedel, R., Eltner, A., 2026. AI image-based method for a robust automatic real-time water level monitoring: a long-term application case. Hydrology and Earth System Sciences 30, 797–824. doi:10.5194/hess-30-797-2026.

Bürkner, P.C., 2017. brms: An r package for bayesian multilevel models using stan. Journal of Statistical Software 80, 1–28. doi:10.18637/jss.v080.i01.

Bürkner, P.C., Vuorre, M., 2019. Ordinal regression models in psychology: A tutorial. Advances in Methods and Practices in Psychological Science 2, 77–101. doi:10.1177/2515245918823199.

Cao, X., Wang, B., Yao, Y., Zhang, L., Xing, Y., Mao, J., Zhang, R., Fu, G., Borthwick, A.G., Qin, H., 2025. U-rnn high-resolution spatiotemporal nowcasting of urban flooding. Journal of Hydrology 659, 133117. doi:10.1016/j.jhydrol.2025.133117.

Cardoso, M.A., Almeida, M.C., Brito, R.S., Gomes, J.L., Beceiro, P., Oliveira, A., 2020. 1d/2d stormwater modelling to support urban flood risk management in estuarine areas: Hazard assessment in the dafundo case study. Journal of Flood Risk Management 13, e12663. doi:10.1111/jfr3.12663.

Cea, L., Sañudo, E., Montalvo, C., Farfán, J., Puertas, J., Tamagnone, P., 2025. Recent advances and future challenges in urban pluvial flood modelling. Urban Water Journal 22, 149–173. doi:10.1080/1573062X.2024.2446528.

Costa, R., Bolte, E., Sharp, C., Bowers, C., 2024. Repeated and localized flooding is an underestimated challenge for urban disaster risk management. Nature Cities 1, 587–596. doi:10.1038/s44284-024-00107-8.

Cristiano, E., ten Veldhuis, M.C., van de Giesen, N., 2017. Spatial and temporal variability of rainfall and their effects on hydrological response in urban areas – a review. Hydrology and Earth System Sciences 21, 3859–3878. doi:10.5194/hess-21-3859-2017.

Dale, J.E., Dorosin, S., Constantine, J.A., Masteller, C.C., 2026. Community-scale urban flood monitoring through fusion of time-lapse imagery, terrestrial lidar, and remote sensing data. Hydrology and Earth System Sciences 30, 2183–2206. doi:10.5194/hess-30-2183-2026.

Delaney, P., 2018. Technical Guideline: MIKE FLOOD Modelling Approaches for Floodplain Mapping. Technical Guideline. DHI Water and Environment Inc.. Cambridge, Ontario, Canada. URL: https://trcaca.s3.ca-central-1.amazonaws.com/app/uploads/2023/02/03175840/Technical-Guideline_MIKE-FLOOD-modelling-Approaches-for-Floodplain-Mapping.pdf. prepared for Toronto and Region Conservation Authority.

Dong, B., Xia, J., Zhou, M., Li, Q., Ahmadian, R., Falconer, R.A., 2022. Integrated modeling of 2d urban surface and 1d sewer hydrodynamic processes and flood risk assessment of people and vehicles. Science of The Total Environment 827, 154098. doi:10.1016/j.scitotenv.2022.154098.

Fappiano, F., Maurer, M., Leitão, J.P., 2026. Data resolution and model complexity in pluvial flood risk assessment: Insights and trade-offs. Journal of Flood Risk Management 19, e70187. doi:10.1111/jfr3.70187.

Gabry, J., Cesnovar, R., Johnson, A., Bronder, S., 2024. cmdstanr: R Interface to 'CmdStan'. URL: https://mc-stan.org/cmdstanr/. r package version 0.8.0.

Guo, K., Guan, M., Yu, D., 2021. Urban surface water flood modelling – a comprehensive review of current models and future challenges. Hydrology and Earth System Sciences 25, 2843–2860. doi:10.5194/hess-25-2843-2021.

Hao, X., Lyu, H., Wang, Z., Fu, S., Zhang, C., 2022. Estimating the spatial-temporal distribution of urban street ponding levels from surveillance videos based on computer vision. Water Resources Management 36, 1799–1812. doi:10.1007/s11269-022-03107-2.

Hedeker, D., Gibbons, R.D., 1994. A random-effects ordinal regression model for multilevel analysis. Biometrics 50, 933–944. doi:10.2307/2533433.

Helmrich, A.M., Ruddell, B.L., Bessem, K., Chester, M.V., Chohan, N., Doerry, E., Eppinger, J., Garcia, M., Goodall, J.L., Lowry, C., Zahura, F.T., 2021. Opportunities for crowdsourcing in urban flood monitoring. Environmental Modelling & Software 143, 105124. doi:10.1016/j.envsoft.2021.105124.

Hossain Anni, A., Cohen, S., Praskievicz, S., 2020. Sensitivity of urban flood simulations to stormwater infrastructure and soil infiltration. Journal of Hydrology 588, 125028. doi:10.1016/j.jhydrol.2020.125028.

Hsueh, H.F., Guthke, A., Wöhling, T., Nowak, W., 2022. Diagnosis of model errors with a sliding time-window bayesian analysis. Water Resources Research 58, e2021WR030590. doi:10.1029/2021WR030590.

Huang, Y., Zhang, J., Zheng, F., Jia, Y., Kapelan, Z., Savic, D., 2022. Exploring the performance of ensemble smoothers to calibrate urban drainage models. Water Resources Research 58, e2022WR032440. doi:10.1029/2022WR032440.

Jiang, J., Liu, J., Cheng, C., Huang, J., Xue, A., 2019. Automatic estimation of urban waterlogging depths from video images based on ubiquitous reference objects. Remote Sensing 11. doi:10.3390/rs11050587.

Krebs, G., Kokkonen, T., Setälä, H., Koivusalo, H., 2016. Parameterization of a hydrological model for a large, ungauged urban catchment. Water 8. doi:10.3390/w8100443.

Leandro, J., Schumann, A., Pfister, A., 2016. A step towards considering the spatial heterogeneity of urban key features in urban hydrology flood modelling. Journal of Hydrology 535, 356–365. doi:10.1016/j.jhydrol.2016.01.060.

Liu, J., Shao, W., Xiang, C., Mei, C., Li, Z., 2020. Uncertainties of urban flood modeling: Influence of parameters for different underlying surfaces. Environmental Research 182, 108929. doi:10.1016/j.envres.2019.108929.

Lyu, H., Zhou, S., Wang, Z., Fu, G., Zhang, C., 2025. Assessing large multimodal models for urban floodwater depth estimation. Water Resources Research 61, e2024WR039494. doi:10.1029/2024WR039494.

Löwe, R., Böhm, J., Jensen, D.G., Leandro, J., Rasmussen, S.H., 2021. U-flood – topographic deep learning for predicting urban pluvial flood water depth. Journal of Hydrology 603, 126898. doi:10.1016/j.jhydrol.2021.126898.

McCullagh, P., 1980. Regression models for ordinal data. Journal of the Royal Statistical Society: Series B (Methodological) 42, 109–127. doi:10.1111/j.2517-6161.1980.tb01109.x.

Ming, X., Liang, Q., Jiang, J., 2025. Large-scale high-resolution hydrodynamic modelling of urban floods: Some practical considerations. Journal of Hydro-environment Research 59, 100655. doi:10.1016/j.jher.2025.100655.

Montalvo, C., Reyes-Silva, J.D., Sañudo, E., Cea, L., Puertas, J., 2024. Urban pluvial flood modelling in the absence of sewer drainage network data: a physics-based approach. Journal of Hydrology 634, 131043. doi:10.1016/j.jhydrol.2024.131043.

Mydlarz, C., Sai Venkat Challagonda, P., Steers, B., Rucker, J., Brain, T., Branco, B., Burnett, H.E., Kaur, A., Fischman, R., Graziano, K., Krueger, K., Hénaff, E., Ignace, V., Jozwiak, E., Palchuri, J., Pierone, P., Rothman, P., Toledo-Crow, R., Silverman, A.I., 2024. Floodnet: Low-cost ultrasonic sensors for real-time measurement of hyperlocal, street-level floods in new york city. Water Resources Research 60, e2023WR036806. doi:10.1029/2023WR036806.

Notarangelo, N.M., Wirion, C., van Winsen, F., 2025. Sturm-flooddepth: A deep learning pipeline for mapping urban flood depth using street-level and oblique aerial imagery. Geomatica 77, 100061. doi:10.1016/j.geomat.2025.100061.

Notti, D., Giordan, D., Caló, F., Pepe, A., Zucca, F., Galve, J.P., 2018. Potential and limitations of open satellite data for flood mapping. Remote Sensing 10. doi:10.3390/rs10111673.

Ochoa-Rodriguez, S., Wang, L.P., Gires, A., Pina, R.D., Reinoso-Rondinel, R., Bruni, G., Ichiba, A., Gaitan, S., Cristiano, E., van Assel, J., Kroll, S., Murlà-Tuyls, D., Tisserand, B., Schertzer, D., Tchiguirinskaia, I., Onof, C., Willems, P., ten Veldhuis, M.C., 2015. Impact of spatial and temporal resolution of rainfall inputs on urban hydrodynamic modelling outputs: A multi-catchment investigation. Journal of Hydrology 531, 389–407. doi:10.1016/j.jhydrol.2015.05.035. hydrologic Applications of Weather Radar.

OpenAI, 2025. GPT-5 model. URL: https://platform.openai.com/docs/models/gpt-5. openAI API model documentation; accessed for the GPT-5 snapshot list including gpt-5-2025-08-07.

Pathirana, A., Tsegaye, S., Gersonius, B., Vairavamoorthy, K., 2011. A simple 2-d inundation model for incorporating flood damage in urban drainage planning. Hydrology and Earth System Sciences 15, 2747–2761. doi:10.5194/hess-15-2747-2011.

Patro, S., Chatterjee, C., Mohanty, S., Singh, R., Raghuwanshi, N.S., 2009. Flood inundation modeling using MIKE FLOOD and remote sensing data. Journal of the Indian Society of Remote Sensing 37, 107–118. doi:10.1007/s12524-009-0002-1.

Pedersen, A.N., Brink-Kjær, A., Mikkelsen, P.S., 2022. All models are wrong, but are they useful? assessing reliability across multiple sites to build trust in urban drainage modelling. Hydrology and Earth System Sciences 26, 5879–5898. doi:10.5194/hess-26-5879-2022.

Pirone, D., Padulano, R., Del Giudice, G., 2026. Approaching urban flood modelling according to available data: A state-of-the-art review and future challenges. Journal of Flood Risk Management 19, e70184. doi:10.1111/jfr3.70184.

Qi, M., Huang, H., Liu, L., Chen, X., 2020. Spatial heterogeneity of controlling factors' impact on urban pluvial flooding in cincinnati, us. Applied Geography 125, 102362. doi:10.1016/j.apgeog.2020.102362.

Riffler, M., Leitner, A., Ralser, S., Poglitsch, E., Schleicher, C., Faucqueur, L., Pennec, A., Marconcini, M., Esch, T., Julea, A.M., Kemper, T., Politis, P., Melchiorri, M., 2025. EMC-BUILT R2025A – Exposure Mapping Component built-up surface grid, derived from Sentinel-2 year 2022. European Commission, Joint Research Centre (JRC). doi:10.2905/b8e9d5a5-8d2a-427d-be3d-0b4dd533bf4f. dataset.

Rosenzweig, B.R., Herreros Cantis, P., Kim, Y., Cohn, A., Grove, K., Brock, J., Yesuf, J., Mistry, P., Welty, C., McPhearson, T., Sauer, J., Chang, H., 2021. The value of urban flood modeling. Earth's Future 9, e2020EF001739. doi:10.1029/2020EF001739.

Shahed Behrouz, M., Zhu, Z., Matott, L.S., Rabideau, A.J., 2020. A new tool for automatic calibration of the storm water management model (swmm). Journal of Hydrology 581, 124436. doi:10.1016/j.jhydrol.2019.124436.

Shastry, A., Carter, E., Coltin, B., Sleeter, R., McMichael, S., Eggleston, J., 2023. Mapping floods from remote sensing data and quantifying the effects of surface obstruction by clouds and vegetation. Remote Sensing of Environment 291, 113556. doi:10.1016/j.rse.2023.113556.

Singh, R., Archfield, S., Wagener, T., 2014. Identifying dominant controls on hydrologic parameter transfer from gauged to ungauged catchments – a comparative hydrology approach. Journal of Hydrology 517, 985–996. doi:10.1016/j.jhydrol.2014.06.030.

Smith, M., Patrick, N., Frazier, N., Kim, J., 2021. Validation of urban flood inundation models applied using nationally available data sets: Novel analyses of observed high water information. Journal of Hydrologic Engineering 26, 04021042. doi:10.1061/(ASCE)HE.1943-5584.0002129.

Songchon, C., Wright, G., Beevers, L., 2021. Quality assessment of crowdsourced social media data for urban flood management. Computers, Environment and Urban Systems 90, 101690. doi:10.1016/j.compenvurbsys.2021.101690.

Tao, Y., Tian, B., Adhikari, B.R., Zuo, Q., Luo, X., Di, B., 2024. A review of cutting-edge sensor technologies for improved flood monitoring and damage assessment. Sensors 24. doi:10.3390/s24217090.

Taylor, J.E., Rousselet, G.A., Scheepers, C., Sereno, S.C., 2023. Rating norms should be calculated from cumulative link mixed effects models. Behavior Research Methods 55, 2175–2196. doi:10.3758/s13428-022-01814-7.

Techapinyawat, L., Goulden-Brady, I., Garcia, H., Zhang, H., 2023. Aerial characterization of surface depressions in urban watersheds. Journal of Hydrology 625, 129954. doi:10.1016/j.jhydrol.2023.129954.

Moy de Vitry, M., Kramer, S., Wegner, J.D., Leitão, J.P., 2019. Scalable flood level trend monitoring with surveillance cameras using a deep convolutional neural network. Hydrology and Earth System Sciences 23, 4621–4634. doi:10.5194/hess-23-4621-2019.

Wan, J., Qin, Y., Shen, Y., Yang, T., Yan, X., Zhang, S., Yang, G., Xue, F., Wang, Q.J., 2024. Automatic detection of urban flood level with yolov8 using flooded vehicle dataset. Journal of Hydrology 639, 131625. doi:10.1016/j.jhydrol.2024.131625.

Wang, W., Yang, S., Stanley, H.E., Gao, J., 2019. Local floods induce large-scale abrupt failures of road networks. Nature Communications 10, 2114. doi:10.1038/s41467-019-10063-w.

Wang, Y., Chen, A.S., Fu, G., Djordjević, S., Zhang, C., Savić, D.A., 2018. An integrated framework for high-resolution urban flood modelling considering multiple information sources and urban features. Environmental Modelling & Software 107, 85–95. doi:10.1016/j.envsoft.2018.06.010.

Wang, Y., Shen, Y., Salahshour, B., Cetin, M., Iftekharuddin, K., Tahvildari, N., Huang, G., Harris, D.K., Ampofo, K., Goodall, J.L., 2024. Urban flood extent segmentation and evaluation from real-world surveillance camera images using deep convolutional neural network. Environmental Modelling & Software 173, 105939. doi:10.1016/j.envsoft.2023.105939.

Xing, Y., Liang, Q., Wang, G., Ming, X., Xia, X., 2019. City-scale hydrodynamic modelling of urban flash floods: the issues of scale and resolution. Natural Hazards 96, 473–496. doi:10.1007/s11069-018-3553-z.

Yang, Q., Huang, H., Wang, C., Lei, X., Feng, T., Zuo, X., 2023. Improving the accuracy of urban waterlogging simulation: A novel computer vision-based digital elevation model refinement approach for roads and densely built-up areas. Remote Sensing 15. doi:10.3390/rs15204915.

Yin, J., Yu, D., Yin, Z., Liu, M., He, Q., 2016. Evaluating the impact and risk of pluvial flash flood on intra-urban road network: A case study in the city center of shanghai, china. Journal of Hydrology 537, 138–145. doi:10.1016/j.jhydrol.2016.03.037.

Yu, J., Li, Y., Huang, X., Ye, X., 2025. Data quality and uncertainty issues in flood prediction: a systematic review. International Journal of Digital Earth 18, 2495738. doi:10.1080/17538947.2025.2495738.

Zahura, F.T., Goodall, J.L., Sadler, J.M., Shen, Y., Morsy, M.M., Behl, M., 2020. Training machine learning surrogate models from a high-fidelity physics-based model: Application for real-time street-scale flood prediction in an urban coastal community. Water Resources Research 56, e2019WR027038. doi:10.1029/2019WR027038.

Zamanizadeh, M., Cetin, M., Shahabi, A., Tahvildari, N., 2025. Depth estimation in urban flooding using surveillance cameras and high-resolution lidar data. Environmental Modelling & Software 192, 106572. doi:10.1016/j.envsoft.2025.106572.

Zhou, S., Lyu, H., 2026. Code and derived data for "sparse validation can mask process errors in urban flood modelling: evidence from large multimodal model-assisted video observations". Zenodo. doi:10.5281/zenodo.21728327. version v1.0.0.